

Role of Copper on L₁₂ Precipitation Strengthened *fcc* based High Entropy Alloy

Bharat Gwalani^{1,2}, Stéphane Gorsse^{3,4}, Vishal Soni², Matthew Carl², Nathen Ley², Aditya V. Ayyagari², Yufeng Zheng⁵, Marcus Young², Rajiv S. Mishra^{1,2} and R. Banerjee^{1,2}

¹Advanced Materials and Manufacturing Processes Institute, University of North Texas
Denton, TX-76207, USA

²Department of Materials Science and Engineering, University of North Texas
Denton, TX-76207, USA

³CNRS, ICMCB, UMR 5026, 33600 Pessac, France

⁴Bordeaux INP, ENSCBP, 33600 Pessac, France

⁵Department of Materials Science and Engineering, The Ohio State University,
Columbus, OH 4310, USA

*Corresponding Author: Raj.Banerjee@unt.edu

Abstract

A novel face-centered cubic (*fcc*)-based precipitation-hardenable high entropy alloy (HEA) or more broadly termed complex concentrated alloy (CCA) has been designed by coupling the beneficial effects of adding small amounts of Ti and Cu to the base alloy, Al_{0.3}CoCrFeNi. While previous work has shown that large concentrations of Cu in *fcc* HEAs based on CoCrFeNi can lead to embrittlement, the present study clearly shows that in small amounts this alloying element can be quite beneficial, since Cu stabilizes the ordered L₁₂ (gamma prime) phase, and acts as a heterogeneous nucleation site for this ordered phase within the *fcc* matrix. Additionally, Ti also stabilizes the L₁₂ phase, increasing its volume fraction. This novel precipitation-hardened HEA/CCA, with a nominal composition of Al_{0.3}Cu_{0.3}Ti_{0.2}CoCrFeNi, exhibits engineering yield and ultimate tensile strengths of 820 MPa and 1100 MPa at room temperature respectively, while

retaining a tensile ductility of nearly 20% and an extraordinarily high strain hardening rate ~ 2700MPa, a rather unique balance of properties for an *fcc*-based austenitic alloy.

Keywords: high entropy alloy, Cu clusters, precipitation strengthening, atom probe tomography

1. Introduction

High strength materials with optimum ductility and thermal stability are always desirable for alloy development and scientific interest. Conventional alloys have one major alloying element, which serves as a matrix (solvent), and other minor additions form the solute or help in precipitation of secondary phases, which can modify the local stress fields leading to the obstruction of the dislocation motion and ultimately resulting in strengthening of the material. In the past few years, a new alloying strategy with equiatomic multi-element alloys or high entropy alloys (HEAs) have attracted enormous scientific attention. HEAs are an intriguing new class of metallic materials which offer a versatile range of permutations of composition and phase structures with a wide range of structure-property combinations [1-8]. This new class of alloys contain high concentrations of four or more elements mixed to form simple phase structures.

Previous reports have clearly demonstrated the potential of precipitation strengthening in *fcc* based HEAs, such as the alloy Al_{0.3}CoCrFeNi, employing ordered L1₂ precipitates as the strengthening phase [8-13]. Additionally, the *fcc* solid solution phase of the same alloy also exhibits a strong dependence of strength on grain size and a very high Hall-Petch hardening coefficient [14]. In addition to Al, additions of Ti, Mo, Nb and Cu to the quaternary CoCrFeNi alloy and in some cases to the Al_{0.3}CoCrFeNi alloy have also exhibited precipitation strengthening [15-22]. Apart from precipitation strengthening, Al_{0.3}CoCrFeNi alloy has also shown promising properties with respect

to radiation tolerance, high velocity deformation, corrosion properties etc. [23-28]. While most of the reports in the literature largely focused on the room temperature mechanical properties of HEAs with ordered intermetallic phases, there is a potential that such precipitation strengthened HEAs may be utilized in high temperature applications, especially since the strengthening ordered intermetallic phases are largely the same as those in present generation high temperature alloys. For example, Ni–Ti–Al-based alloys with intermetallic phases, like Ni_3Al (Strukturbericht L₁₂) based on the ordered face-centered cubic (*fcc*), NiAl (Strukturbericht B₂) based on the ordered body-centered cubic (*bcc*) and the Huesler phase Ni_2AlTi (Strukturbericht L₂₁) based ordered *bcc*, have found applications in aircraft engines. Among the ordered *bcc* phases in Ni–Al–Ti alloys, the L₂₁ phase has higher creep resistance than B₂ because of the presence of limited slip systems in L₂₁ [29].

The $\text{Al}_{0.3}\text{CoCrFeNi}$ *fcc* HEA was originally developed as a precipitation strengthenable system by marginally increasing the Al content in the original single-phase solid solution $\text{Al}_{0.1}\text{CoCrFeNi}$ *fcc* HEA [1]. While the $\text{Al}_{0.3}\text{CoCrFeNi}$ *fcc* HEA is in some ways a model system for investigating precipitation-strengthening in HEAs and offers a reasonable balance of tensile strength and ductility, it is not optimized composition for precipitation strengthening. The coherent nano-precipitates based on the L₁₂ structure (gamma prime like, γ') have a relatively low phase fraction and dissolution temperature (<700°C) in this alloy [30]. Therefore, in order to develop a high strength thermally stable material retaining a large fraction of strengthening nano-precipitates it is necessary to optimize the composition.

The current alloy - $\text{Al}_{0.3}\text{Cu}_{0.3}\text{Ti}_{0.2}\text{CoCrFeNi}$ (6.5% Al, 6.5% Cu, 4.0% Ti, and 20.75% Co, Cr, Fe, Ni each atomic percent) is a modification of $\text{Al}_{0.3}\text{CoCrFeNi}$ alloy with minor additions of Cu and

Ti aimed at increasing the stability of L₁₂ phase at elevated temperatures. Ti is added to Ni-Al-Cr base super-alloys used in gas turbine engines which are strengthened by coherent Ni₃(AlTi) γ' precipitates [31, 32]. In ultrahigh strength maraging steels [33, 34], Ti is introduced to precipitate Ni₃Ti phase in the *fcc* austenitic matrix. Recently, the effect Ti addition to *fcc* based high entropy alloy has been investigated [35, 36]. He et al. [37] showed that small amount of Ti (<5 %) addition to a CoCrFeNi *fcc* matrix can form coherent L₁₂ precipitates consequently leading to substantial improvements in the strength.

There have been relatively fewer investigations on the role of Cu addition to HEAs based on CoCrFeNi. The original studies involving Cu addition were motivated by the possibility of cost-reduction by substituting expensive Co with Cu [38]. However, these alloys typically had a molar ratio of 1 for Al in compositions such as AlCuCrFeNi₂, making them *bcc* based HEAs, rather than *fcc* based. More recently, investigation on a lower Al containing, Al_{0.3}CuCrFeNi₂ alloy [39] suggested that Cu, which readily forms clusters due to its positive enthalpy of mixing with other constituent elements, played a crucial role in stabilizing the L₁₂ precipitates (solvus or dissolution temperature ~930 °C). Additionally, it was observed that the L₁₂ phase appears to be heterogeneously nucleated on clustered Cu-rich regions. A third possible effect is that these Cu clusters could potentially hinder dislocation motion, as claimed in case of Fe-Cu alloys, leading to an increase in the flow stress of these alloys [40, 41].

The present study focuses on the Al_{0.3}Cu_{0.3}Ti_{0.2}CoCrFeNi *fcc*-based HEA. This specific composition was chosen based on three considerations. Small additions of Al, Ti and Cu can (1) stabilize coherent L₁₂ precipitates in the CoCrFeNi single *fcc*-phase, (2) increase the L₁₂ phase fraction by appropriately tailoring the amounts of Al, Ti, and Cu, and potentially increase the

solvus temperature of these precipitates, and (3) additionally form semi-coherent precipitates like B2 or L2₁ on the grain boundary to restrain grain growth by grain boundary pinning [14].

2. Experimental Procedure

An alloy with the nominal chemical composition Al_{0.3}Cu_{0.3}Ti_{0.2}CoCrFeNi (6.25 at% Al + 6.25 at% Cu + 4.1 at% Ti and 20.8 at% Co, Cr, Fe and Ni each) was prepared by a conventional arc-melting route. The ingot was remelted five times for homogenization of the alloy. Subsequently, the alloy was further annealed at 1150°C for 1 h and then cold-rolled to a reduction of 70% in thickness (subsequently referred to as the CR condition). The cold-rolled pieces were recrystallized at 1150°C for 5 mins (for limiting *fcc* grain growth) followed by different precipitation annealing treatments. The cold-rolled plus recrystallized condition will be referred to as the CR-R condition. These treatments included various temperature/time combinations ranging between 600°C – 800°C, but this paper will focus on three critical precipitation annealing treatments, CRR, CR-R+600°C/150h, CR-R + 800°C/0.5h, referred to as *CR-R*, *CR-R-600*, and *CR-R-800* respectively. The entire thermo-mechanical processing route for the alloy has been schematically depicted in Figure 1(a).

Microstructural characterization was performed using scanning electron microscopy (SEM) (FEI Nova-NanoSEM 230TM), coupled with energy dispersive spectroscopy (EDS). The tensile tests were carried out by setting the initial strain rate at 10⁻³ s⁻¹ with respect to change in length. For each test performed, the strain rate variation was noted to be less than 1 % from the desired strain rate. These tests are quasi-static tests which used a linear variable displacement transformer (LVDT) extensometer. The tensile test specimens (gauge length ~ 3 mm, width ~ 1 mm and

thickness \sim 0.5–1 mm) were machined using electric discharge machine (EDM). At least five independent tests were carried out to obtain tensile elongation and strength data.

Conventional transmission electron microscopy (TEM) studies were carried out on a FEI Tecnai G2 TF20TM operating at 200 kV. Precipitate characterization was done using conventional and high angle annular dark field-scanning TEM (HAADF-STEM) modes. To measure the composition, energy dispersive spectroscopy (Super-X system) equipped on an FEI-TITAN G2 TEM microscope was used in the HAADF STEM mode operating at 300 kV and the results were analyzed with FEI's ES vision software version 6. The STEM-EDS maps have been recorded in an aberration-corrected TITAN TEM equipped with a Super-EDS detector, also referred to as the ChemiSTEM technique. TEM foils were prepared by FEI Nova Nanolab 200 dual-beam focused ion beam (FIB) instrument using a Ga ion beam for milling. The ion beam thinning of the samples was done in multiple steps starting from 30 kV ions and finishing with 5 kV ions to reduce the surface damage caused by higher energy ions.

Standard lift-out techniques were used for Atom Probe Tomography (APT) sample preparation in the FIB before mounting the small sections of the samples on suitable holders for analysis. APT experiments were conducted on a CAMECA local electrode atom probe 3000X HR instrument. All experiments were performed in the temperature range of 50 K with target evaporation of 0.5% and pulse fraction of 20% of a steady-state applied DC voltage. APT data reconstruction and analysis were carried out using CAMECA IVAS® 3.6.12 software.

Samples for *ex situ* synchrotron X-ray diffraction (SR-XRD) measurements were prepared with dimensions of $5 \times 5 \times 0.5$ mm³ (thickness). SR-XRD measurements were taken in a transmission geometry at the 11-ID-C beamline (111 keV approximate beam energy, $\lambda = 0.117418$ Å) of the

Advanced Photon Source (APS) at Argonne National laboratory (ANL). A diffraction image for a CeO₂ standard (NIST diffraction intensity standard set: 674a) was collected and then Fit2D software [42] was utilized to calibrate detector parameters such as sample-to-detector distance, beam center, and detector tilt angles. Experimental diffraction patterns were taken with a beam size of 1 x 1 mm² and a total exposure time of 2.5 seconds per diffraction file and collected using Perkin Elmer amorphous Si area detector. Nine diffraction files from different areas of the sample were then summed together to improve statistics for further quantitative analysis producing a single diffraction image representing an irradiated volume of 4.5 mm³ for each sample. Data analysis was performed using a combination of Fit2D, custom MatLab code [43], and MAUD software [44]. Starting phases for the quantitative phase analysis were obtained from the Crystallography Open Database [45] and modified respectively to better fit the properties of the HEA (FCC – COD ID: 9008468 [46, 47], L₂ – COD ID: 5910083 [35, 36], L₁ – COD ID: 5910053 [37, 38], Sigma – COD ID: 2106166 [48, 49].

3. Results and Discussion

3.1 Influence of thermo-mechanical processing on microstructure

Figures 1 (b, c and d) show the micrographs from CR-R, CR-R-600 and CR-R-800 respectively. Note the dark contrast phase on the grain boundary (GB) in all conditions. The GB phase is discontinuous, discrete and has a lower phase fraction, in the CR-R condition (Figure 1 (b)) whereas these grain boundary precipitates are more continuous in the CR-R-600 condition (Figure 1 (c)). The inset in Figures 1(c) shows high magnification image from GB region in CR-R-600, suggesting that the phase fraction of GB phase/phases increases on extended annealing at 600°C. In Figure 1 (d) a low magnification image shows the recrystallized grains in CR-R-800 condition,

nevertheless a higher magnification image in the inset of this figure clearly reveals the grain boundary precipitates. The grain size for the CR-R and CR-R-600 was $\sim 10 \mu\text{m}$, whereas it was $\sim 25 \mu\text{m}$ for CR-R-800 (refer supplementary Figure S1). The structural and compositional details of these phases have been investigated using synchrotron x-ray diffraction (XRD) and TEM-based techniques, and the results will be presented in subsequent sections.

3.2 Phase investigation using synchrotron x-ray diffraction

Synchrotron XRD technique has been employed for capturing all the phases in the two precipitation annealed conditions as well as the cold-rolled and recrystallized condition. The results in Figure 1 (e) show the XRD traces from all three conditions in a staggered-plot. The lower most XRD curve in black color corresponds to the CR-R condition, which shows *fcc* and L2_1 phase peaks. Additional low temperature annealing results in precipitation of other intermetallic phases. For example, in case of CR-R-600 (second from bottom, red color) and CR-R-800 (top, blue color) conditions have extra peaks corresponding to the sigma (σ) and L1_2 (γ') phases. The $\text{B}2$ phase is another possible ordered intermetallic phase that has been reported in $\text{Al}_x\text{CoCrFeNi}$ type HEAs [30]. One important point that should be noted is the possible overlap of diffraction peaks from the L2_1 and $\text{B}2$ phases in these samples. The L2_1 structure is derived from the $\text{B}2$ structure, considering a $2\times 2\times 2$ array of eight adjacent $\text{B}2$ unit cells [51]. Therefore, assuming the L2_1 unit cell with a lattice parameter that is double that of the $\text{B}2$ unit cell, there will be an overlap of most of the prominent peaks from both phases. In fact, all $\text{B}2$ peaks will overlap with those of L2_1 , and there are only a few peaks unique to the L2_1 phase, such as $\{111\}$ and $\{222\}$. Consequently, it is very difficult to establish the presence of $\text{B}2$ and quantify its phase fraction, based on these x-ray diffraction results. Table 1 shows the phase fraction of each phase after various heat treatments,

calculated from the synchrotron XRD results. The phase fractions corresponding to the L₂₁ phase have been designated as L₂₁/B2 due to the potential of peak overlap between these two phases. CR-R-600 has ~34 % L₁₂, ~13 % L₂₁, 10 % sigma and rest *fcc*. L₁₂ was not detected in CR-R condition which has ~6 % L₂₁ and rest *fcc*. CR-R-800 has ~15% L₁₂ phase along with ~4% L₂₁ and ~1% sigma phase. Furthermore, Table 1 also shows the lattice constants of each phase. The lattice mismatch between *fcc* ($a=3.6 \text{ \AA}$) and L₁₂ ($a= 3.6 \text{ \AA}$) appears to be extremely small, indicating a preference to form a coherent interface between them. In addition the L₂₁ phase (*fcc* symmetry) has a lattice parameter of $a = 5.84 \text{ \AA}$ and σ phase with a tetragonal symmetry has $a=8.79 \text{ \AA}$ and $b=4.55 \text{ \AA}$. These alloy conditions have been subsequently investigated in detail to understand the influence of L₁₂ precipitates on the mechanical properties.

3.3 Detailed characterization of as cold-rolled and recrystallized (CR-R) condition

We first focus on the characterization of the CR-R condition. Figure 2(a) shows a bright field (BF) TEM image from a site-specific TEM sample extracted from a grain boundary region in this sample. The grain boundary is marked with white dotted line with a triangular shaped blocky grain boundary precipitate along it. Figures 2(b-d) show selected area diffraction patterns (SADPs) recorded along three different zone axes from the matrix region, which can be unambiguously indexed as [112], [001] and [011] zone axes of a disordered *fcc* phase, respectively.

Figures 2 (e-f) shows the SADPs from two different zone axes of the grain boundary precipitate. These two diffraction patterns can be indexed as the [011] and [001] zone axes of a *bcc* type ordered crystal structure. The presence of 1/4, 2/4, 3/4 {222} spots in the [011] zone axis establishes the phase to be an ordered L₂₁, rather than B2. The existence of extra (-11-1) and (-1-11) reflections in Figure 2 (e) are inconsistent with B2 ordering which has a symmetry of Pm-3m.

However, the presence of these reflections is consistent with the Fm-3m symmetry observed for the [110] zone of an ordered L₂₁ structure (Huesler structure, fm-3m).

Figure 2 (g) shows a dark field TEM (DFTEM) image, where the GB precipitate exhibits the brighter contrast. This dark-field image was recorded using a super-lattice reflection in the [001] L₂₁ zone axis, marked by the dashed yellow circle in Figure 2 (f), and this image unambiguously confirms that there are L₂₁ precipitates decorating the grain boundary in this alloy. Recent reports indicate that addition of Ti could stabilize the L₂₁ phase in high entropy alloys [37, 51]. Figure 2 (h) shows a high-angle annular dark-field (HAADF) STEM from this region of the sample and the corresponding STEM-EDS maps of various elements are displayed in Figures 2 (i-o). The grain boundary phase is found to be enriched in Al, Ti, and Ni, while being depleted of Cr and Fe. Cu and Co do not partition between the matrix and precipitate as strongly as the other elements. However, one cannot rule out the possibility of additional B2 precipitates at the grain boundaries.

Figure 3 shows the atom probe tomography (APT) results from the matrix of the CR-R condition. The ion maps for the different elements have been shown in the figure and have been labeled in Figure 3. Visual inspection does not reveal any significant compositional inhomogeneity within the *fcc* matrix in this condition. A 1-D compositional profile, averaged along a cylindrical cross-section (radius = 10 nm, length = 400 nm), along the axis of the APT reconstruction, has been shown in Figure 3 (b). The 1-D profile does not show any major composition fluctuations, further establishing clear compositional homogeneity. Cu containing HEAs have been shown to readily form Cu rich clusters due to a large positive enthalpy of mixing of Cu with the other elements [39]. The current alloy condition (CR-R) does not show any significant partitioning of Cu possibly due to the prior cold rolling followed by recrystallization annealing.

3.4 Detailed characterization of cold-rolled plus precipitation annealed at 600°C/150h (CR-R-600) condition

Careful microstructural examination of the CR-R-600 using TEM and APT allowed us to characterize the matrix and GB phases in detail. Figures 4 and 5 show the results from the TEM investigations. Figures 4 (a and b) show the SADPs recorded from the $[011]_{fcc}$ and $[001]_{fcc}$ zone axes of the matrix. The SADPs show the presence of extra super-lattice spots at $\{001\}$ positions in the $[001]$ zone and $\{001\}$ and $\{011\}$ positions in the $[011]$ zone, clearly establishing the presence of ordered $L1_2$ precipitates in the fcc matrix. These $L1_2$ precipitates are clearly shown in the dark field image (Figure 4 (c)) recorded from the $\{001\}$ super-lattice spot highlighted by a red circle in Figure 4 (a). The $L1_2$ precipitates appear to range in size from 10-20 nm. The compositional partitioning of elements within the matrix is shown in the STEM EDS maps in Figures 4 (d-g). The elemental maps of Ni (cyan), Al (red), Cr (blue) and Cu (orange) are shown as labeled in Figures 4(d-g). It is noteworthy that the Al, Ni and Cu partition into the $L1_2$ phase. Furthermore, an additional Cu rich phase, with a higher Cu content as compared to the $L1_2$ precipitates, was also observed in the microstructure. These Cu-rich regions appeared to be associated with the $L1_2$ precipitates. Further detailed analysis of the $L1_2$ precipitates and the Cu rich phase had been carried out using APT and the results will be discussed in a subsequent section.

Figure 5 shows the TEM and STEM results from the grain boundary precipitates in the CR-R-600 condition. Figures 5 (a-f) shows the HAADF-STEM image, and ChemiSTEM EDS maps for Cu, Fe, Ni, Al and Cr elements, respectively, from the GB region. Based on the STEM EDS analysis it appears that there are at least four compositionally distinct phases in this region. The crystal structures of the GB precipitates have been characterized using microdiffraction in the TEM.

Figures 5 (g-i) show the diffraction patterns from the [011] L₂₁, [011] bcc and [221] σ phases, respectively. Comparing the EDS compositional maps and the diffraction patterns, it appears that the L₂₁ phase is enriched in Al, Ti, and Ni, the disordered bcc phase is enriched in Cr, and the σ phase is enriched in Cr and Fe. Again, in this case, one cannot rule out the possibility of some B2 precipitates at the grain boundary.

A better distinction between the multiple phases present at the grain boundary is enabled by overlaying the elemental STEM maps for the different elements on one plot, as shown in Figure 5 (j). The different grain boundary phases have been labeled in Figure 5 (j) and an arrow (yellow colored) has been marked. 1-D compositional profiles for the different elements, along this arrow, have been plotted in Figure 5 (k). These profiles start from the *fcc* matrix and then sequentially pass through a Cu rich precipitate, a sigma precipitate, a bcc precipitate, and finally end in the matrix region of the adjacent grain. Additionally, Table 2 shows a summary of compositions of these phases (Cu-rich phase, L₁₂, L₂₁, σ phase and *fcc* matrix), acquired by averaging spot EDS measurements. σ precipitation has been previously reported in high Cr steels [52] as well as in high entropy alloys. *In situ* TEM studies by Rao et al. showed precipitation of B2 (Ni-Al based) and σ as a grain boundary precipitate in Al_xCoCrFeNi alloys ($x = \text{Al}_{0.3}$, Al_{0.5} and Al_{0.7}) [53]. Precipitates of the L₂₁ (Ni₂AlTi) phase, which is based on a bcc structure, and the σ phase, based on a tetragonal structure, are difficult to nucleate within an *fcc* matrix, and hence precipitate at the grain boundaries. These grain boundary precipitates can possibly restrict the grain growth and harden the grain boundaries. Tang et al. showed precipitation of B2 in an ultrafine grained *fcc* Al_{0.3}CoCrFeNi alloy resulting in a substantial hardness increment [54].

The fine scale L₁₂ and Cu-rich precipitates within the *fcc* matrix have been investigated in detail using APT. Figure 6 show the APT results from the CR-R-600/150h condition. Figure 6 (a) displays the ions maps of all ions, Al ions, Ni ions, Cu ions, Ti ions, Cr ions and Co ions from left to right on the figure. A clear inhomogeneity can be seen in all the compositional maps. Figure 6 (b) shows the spatial distribution of various precipitates in the matrix at a higher resolution. A 25 at% Cu (orange) and 15% Al (cyan) iso-concentration surface (also referred to as iso-surface) have been used to delineate the Cu-rich regions, L₁₂ precipitates, and the matrix as shown in a 100nm x 40nm x 10nm slice of the 3D reconstruction in Figure 6 (b), with Cr atoms shown in green color representing matrix region. The close proximity of the Cu-rich regions with the L₁₂ precipitates is evident in this three-dimensional APT reconstruction of the microstructure, in agreement with the two-dimensional STEM-EDS maps shown in Figures 4 (d-g), for the same condition. Figures 6 (b, right side) shows the proximity histograms depicting the compositional partitioning across the various interfaces viz. the L₁₂/matrix and the Cu-rich phase/matrix interfaces In addition, Table 3 shows the composition of each phase obtained by placing a sphere of 5nm diameter within each phase and measuring the composition of the volume enclosed within the sphere.

3.5 Detailed characterization of the cold-rolled plus precipitation annealed at 800°C/0.5h (CR-R-800) condition

The synchrotron XRD results show that the L₁₂ phase is also observed in the CR-R-800 condition (similar to CR-R-600 condition). Figure 7 summarizes the TEM and STEM-EDS observations from this condition. Figure 7 (a) shows a low magnification dark-field TEM image from an intra-granular region, recorded from a {100} super-lattice reflection, corresponding to the L₁₂ phase, in the [001] *fcc* zone axis diffraction pattern (shown as an inset in the same figure). The specific

super-lattice reflection used for recording this dark-field image, has been marked with a red circle in the inset diffraction pattern. There is a high number density of fine scale L₁₂ precipitates, highlighted in this dark-field image. Interestingly, there appears to be an alignment of the ordered L₁₂ precipitates along the <001>*fcc* direction when the TEM foil is oriented along the [001] zone axis. Such a strong alignment of the L₁₂ precipitates was not observed when the same sample is imaged along other *fcc* zone axes. Figure 7 (b) shows a higher magnification dark-field TEM image, recorded along the [011]*fcc* zone axis, using a {100} super-lattice reflection (marked with a yellow circle in the diffraction pattern shown as an inset). The L₁₂ precipitates are clearly highlighted in this dark-field image. Additionally, this image also contains a twin boundary in the *fcc* matrix, as evidenced from the additional set of *fcc* matrix spots, present in the [011]*fcc* zone axis diffraction pattern, arising from the reflection of matrix spots about the common g={111} reciprocal lattice vector. This twin boundary has also been marked on the dark-field image in Figure 7 (b).

The alignment of L₁₂ precipitates along the <100> directions, when imaged along the [001]*fcc* zone axis, suggests the possibility that a phase separation reaction via spinodal decomposition preceded or took place concurrently with the L₁₂ ordering reaction. Assuming that the spinodal decomposition preceded the ordering reaction, a possible transformation pathway would be that initially the *fcc* phase separated into *fcc*1 and *fcc*2 phases. Subsequently, one of the *fcc* phases undergoes an ordering transformation to form the L₁₂ phase. Such concomitant phase separation and ordering transformations in alloys have been previously reported [55]. Assuming that phase separation occurs via spinodal decomposition, the compositional waves are likely to be along the elastically soft <100> directions in the *fcc* matrix, and the interference of these waves along the three crystallographically degenerate <100> directions would likely result in two compositionally

distinct types of pockets. Subsequently, the pockets rich in Al and Ni undergo an ordering transformation to form L₁₂ (Ni₃Al type) precipitates, whereas the other pockets rich in Fe, Cr and Co remain disordered. While this proposed decomposition mechanism could potentially explain the alignment of the L₁₂ precipitates along the <100> directions, the post-deformation experimental observations presented in this paper are not sufficient for conclusively deciphering the transformation pathway.

Furthermore, near the *fcc* matrix grain boundaries in the CR-R-800 condition, discontinuous precipitation of L₁₂ phase was observed in the form of a lamellar L₁₂+*fcc* product. This is shown in the dark-field TEM image shown in Figure 7 (c), recorded from the same {100} super-lattice spot highlighted in the [011]*fcc* zone shown in the inset of Figure 7 (b). The corresponding STEM-EDS maps for the different elements, recorded in the grain boundary region exhibiting the discontinuous precipitation, are shown in Figure 7 (d-j). Within the lamellar discontinuous product forming at the grain boundary, the ordered L₁₂ phase is enriched in Ni, Al, and Ti, while the disordered *fcc* regions are enriched in Fe, Cr, Co, and Cu. Interestingly, the Cu enrichment appears to be largely confined to the *fcc* lamellae in the vicinity of the grain boundary, but does not permeate into the adjacent continuous *fcc* matrix of the grain. Such heterogeneous formation of discontinuous L₁₂ (γ') precipitates at the grain boundaries had been previously reported in Ni-base super-alloys on annealing at high temperatures [56, 57]. Annealing at a high temperature, such as 800°C, results in a close competition between homogenous nucleation of γ' within the matrix, versus heterogeneous discontinuous precipitation of γ' precipitates at grain boundaries. The driving force for γ' precipitation is relatively lower at higher temperatures, due to the lower undercooling below the γ' solvus temperature, consequently lowering the homogenous nucleation

rate. Under these circumstances, both grain boundary formation of discontinuous γ' and intra-granular precipitation of homogeneously nucleated γ' is observed [56, 57].

3.6 Thermodynamic modeling of phase stability in $Al_{0.3}Cu_{0.3}Ti_{0.2}CoCrFeNi$

Solution thermodynamic computations of the Al-Cu-Ti-Co-Cr-Fe-Ni septenary system have been carried out for the relevant compositional ranges and temperatures, using CALPHAD based ThermoCalc and the TCHEA2.1 database specifically developed for HEAs. The complex phase stability regimes for this system have been depicted in the two-dimensional (2D) sections at $(Al,Cu,Ti)0.8$ for this septenary system in Figures 8 (a) and (b), corresponding to 600°C and 800°C, respectively. The specific alloy composition chosen in the present study, $Al_{0.3}Cu_{0.3}Ti_{0.2}CoCrFeNi$, has been marked with red circles in both these isothermal sections. It falls in the $\sigma + L1_2 + B2\#1 + B2\#2 + fcc\#1$ and $fcc\#2 + B2\#1 + \sigma + L1_2 + fcc\#1$ phase field at 600°C and 800°C, respectively. Due to the compositional complexity of this seven-component system, the development of robust thermodynamic models for the individual phases is rather challenging. A complete thermodynamic database for a septenary system would require 21 binary and 35 ternary system descriptions. The TCHEA2.1 database includes complete thermodynamics for all the binary systems and 18 fully assessed ternaries which give a fraction of assessed binaries FAB = 1 and a fraction of assessed ternaries FAT = 0.51. The obtained values of these credibility metrics developed by Senkov et al. suggest that prediction capability of the TCHEA2.1 database **is limited** for the current septenary alloy. Additionally, the number of possible phases increases, and so does the competition between these phases in terms of thermodynamic stability. Therefore, the results of the thermodynamic modeling presented in this paper have only been used as a

guideline to rationalize the experimentally observed phases at the two different temperatures, 600°C and 800°C.

Figure 9 (a) shows the phase fraction (mole fraction) of the different equilibrium phases as a function of temperature for the specific alloy composition. While the synchrotron x-ray diffraction results only revealed the presence of *fcc*, L₁₂, L₂₁/B2 and σ phases after long term annealing at 600°C, the more detailed TEM investigation revealed the presence of grain boundary *bcc* phases (refer to Figure 5). The *fcc*, L₁₂ and σ phases are predicted and experimentally observed at both 600°C and 800°C. However, it is rather interesting to note that the experimentally measured (synchrotron x-ray diffraction) L₂₁/B2 phase fraction in this alloy after 600°C/150h annealing was determined to be 13%, while ThermoCalc does not predict the presence of any equilibrium L₂₁ phase at 600°C. Rather the thermodynamic modeling predicts two different B2 phases, with phase fractions of 18% and 16% respectively. Delving further into this issue, the thermodynamic onset driving forces for the different phases have also been evaluated and these results are shown in Figure 9 (b). The driving force for L₁₂ precipitation is the maximum at both temperatures, followed by that for the B2/*bcc* phase, then the L₂₁ phase, and finally the lowest driving force is for the σ phase. Thus, it is evident that there is a substantial driving force for the L₂₁ phase, though this might be superseded by the driving force for precipitation of the B2/*bcc* phase. Accounting for the fact that it is experimentally difficult to distinguish the phase fractions of L₂₁ and B2 phases, due to the large number of overlapping peaks in the x-ray diffraction patterns, the L₂₁/B2 precipitation trends predicted by ThermoCalc are reasonable though the actual phase fractions do not exactly concur. Furthermore, it should be noted that the experimental results may not reflect the true equilibrium condition of this alloy, arising from the system's inability to achieve equilibrium due to kinetic constraints.

At a temperature of 800°C, ThermoCalc predicts a *fcc*#2 + B2#1 + σ + L1₂ + *fcc*#1 phase equilibria, *fcc*#2 and *fcc*#1 being (Fe,Co,Cr)-rich and Cu-rich (90at.%) according simulations, respectively. Comparing with the experimental results it appears that the two *fcc* phases predicted at this temperature, are the matrix *fcc* solid solution, and the Cu-rich *fcc* phase. The Cu-rich *fcc* phase appears to precipitate in a discontinuous manner together with the L1₂ phase, at the grain boundaries of the *fcc* matrix, as seen in Figure 7 (note the STEM-EDS Cu map). Additionally, finer scale *fcc* Cu-rich precipitates may be associated with the homogeneously precipitating intra-granular L1₂ precipitates, comparable to the observations in case of the 600°C annealed sample. Comparing the predicted phase fractions with the experimentally observed phase fractions (based on the synchrotron x-ray diffraction results) at 600°C, the predicted phase fractions of L1₂ and σ are 24% and 34.6% respectively, while the experimentally observed values are 34.2% and 10.1% respectively. This difference can be attributed to the coupled effects of sluggish diffusion kinetics at 600°C preventing the alloy from achieving true equilibrium as well as inaccuracies associated with solution thermodynamic models used for the predictions (FAT = 0.51). On the other hand, at 800°C, the predicted phase fractions of L1₂ and σ are 14.8% and 19.6% respectively, while the experimentally observed values are 15.3% and 1% respectively. The lower phase fraction of the σ phase in both cases is due to the high nucleation barrier for this phase, as compared to much lower nucleation barrier for the L1₂ phase within the *fcc* matrix.

Summarizing, the simulated equilibrium phase diagram of such complex concentrated alloys involving the 3D transition elements (Co, Cr, Fe, Ni, Cu) together with small additions of Al and Ti only partially supports the experimental observations. It explains the formation of the *fcc*, L1₂, σ and Cu-rich phases in the microstructure of the septenary alloy after annealing and afford reasonable predictions of the precipitation trends. However, it fails to accurately predict the

observed phase fractions and the L₂₁ phase formation. The pointed discrepancies between simulations and experiments are mainly related to the L₂₁ and σ phases, which can arise from unprecise thermodynamic description of these phases, reducing the reliability of the calculations in this complex septenary alloy system. The L₂₁ phase is modelled using a 3-sublattice model (Al,Cr,Ni,Ti)_{0.5}(Al,Ni;Ti)_{0.5}(Co,Fe,Ni,Al)₁ while measured composition includes 11.53 at.% of Cu. It is likely that the lack Cu solubility in the thermodynamic description of the L₂₁ phase is the main reason why the simulations predict the formation of a B2 phase in place of the L₂₁ phase. Similarly, overestimation of the predicted fraction of the σ phase can arise from the lack of Cu in the sublattice model used to describe the σ phase: (Al,Co,Cr,Fe,Ni,Ti)₁₀(Al,Co,Cr,Fe,Ni,Ti)₄(Al,Co,Cr,Fe,Ni,Ti)₁₆.

3.7 Mechanical Response under Tensile loading

Tensile testing of three different conditions, CR-R, CR-R-600 and CR-R-800, was carried out under quasi-static loading conditions, using strain rates of 10⁻³ sec⁻¹. Figure 10 (a) shows the engineering stress strain curves and Figure 10 (b) shows the true stress-strain curves for these three conditions. Additionally, the respective work hardening rates as a function of strain have been shown as an inset of Figure 10 (b). The CR-R condition exhibits a yield strength (YS), $\sigma_y = 375$ MPa, and an elongation to failure, $\varepsilon_f = 65\%$. Post precipitation annealing treatments, the conditions show an increase in YS reaching $\sigma_y = 720$ MPa in case of the CR-R-800 condition and $\sigma_y = 840$ MPa for the CR-R-600 condition. The increase in strength due to precipitation of the ordered intermetallic L₁₂ phase can be observed clearly in these two cases. Even though the YS of the material increases by nearly 225%, the precipitation strengthened condition exhibits very good tensile ductility. The elongation to failure for the CR-R-800 is $\varepsilon_f = 20\%$ whereas for CR-R-600 it

is $\varepsilon_f = 25\%$. Furthermore, the ultimate tensile strength (UTS) for the CR-R-600 condition, based on the engineering stress-strain curve shown in Figure 10 (a), is ~ 1.1 GPa. The work-hardening rate versus true strain is shown in the inset in Figure 10 (b). The low-SFE *fcc* metals/alloys exhibit a distinct four-stage strain response under simple deformation tests, which very different from the medium and high SFE materials [58]. The four stages of strain hardening are discussed as following in the literature: stage A - with a steadily decreasing strain hardening rate; stage B - with an almost constant strain hardening rate; stage C - with a steadily decreasing strain hardening rate up and a final stage D - again with an almost constant strain hardening rate [58, 59, 60, 61]. The initiation of stage B has been often correlated with the initiation of deformation twinning. Similarly, the initiation of stage D is correlated with extensive twin intersections in the microstructure [59]. The decrease of strain hardening in stage C is due to the decreasing rate of primary twinning. In the current study, the steady-state work-hardening rates, marked as stage B in the work-hardening rate versus true strain, in the inset in Figure 10 (b), are nearly similar for the CR-R and CR-R-800 conditions (~ 1700 MPa), while it is ~ 2800 MPa for the CR-R-600 condition. Both these values of work-hardening rates are very high and a value of ~ 2800 MPa is exceptional for *fcc*-based materials. Overall, the CR-R-600 offers a very promising strength-ductility combination with excellent work hardenability. While the details of the associated deformation mechanisms during tensile loading, for the three conditions discussed in the present study is beyond the scope of the present paper, the exceptional work-hardening rates, especially for the CR-R-600 condition warrant more detailed investigation of the deformed microstructures which will be addressed in the future.

Previously in $\text{Al}_{0.3}\text{CoCrFeNi}$ HEA, a strength increment from ~ 260 MPa to 490 MPa was reported on precipitation of L1_2 precipitates in a $\sim 25 \mu\text{m}$ grain size *fcc* matrix [14]. Another report on an

$\text{Al}_{0.2}\text{Ti}_{0.1}\text{CoCrFeNi}$ alloy showed a strengthening from ~320 MPa to ~650 MPa on precipitation of L1_2 precipitates in a ~18 μm grain size fcc matrix [37]. The current alloy shows an increment of strength from 375 MPa in CR-R condition to 840 MPa in the precipitation annealed CR-R-600 condition. The large increase in strength after precipitation annealing treatment in current alloy can also be attributed to coherent copper clusters in the matrix apart from the L1_2 precipitates. Such clusters can provide additional strengthening to the alloy. Strengthening due to Cu-cluster has also been discussed by many researchers in Cu-bearing steels like those that HSLA-100 used for shipbuilding [40, 41].

4. Summary and Conclusions

Coupling the effects of adding small molar fractions of Al, Ti, and Cu, to the base fcc solid-solution based CoCrFeNi alloy, a new $\text{Al}_{0.3}\text{Cu}_{0.3}\text{Ti}_{0.2}\text{CoCrFeNi}$ HEA has been developed with the objective of exploiting the positive effects of each of these additional alloying elements. Thus, while Al and Ti promote the precipitation of the strengthening nanometer scale L1_2 phase within the fcc matrix, Cu clusters not only provide the nucleation site for L1_2 precipitation but also Cu clusters can strengthen the alloy further. The L1_2 phase is stable at high temperature (800 °C). The L1_2 phase fraction at 600 °C was 34% whereas at 800 °C it was 15 %. A high fraction of L1_2 at 600 °C strengthens the alloy to UTS of 1.1 GPa. The size scale of L1_2 precipitates in CR-R-600 is ~10 nm whereas it is ~35 nm in CR-R-800 condition. The size scale plays a very important role in the strengthenability of the coherent precipitate and hence the CR-R-600 shows much high YS. Furthermore, we notice grain growth in CR-R-800 condition from 10 μm to 25 μm in CR-R-800 condition which could further reduce the YS. Grain boundary precipitation of L2_1 was observed in all three conditions and can possibly act as grain boundary strengthener. Apart from L2_1 , sigma phase is seen in synchrotron XRD and TEM results in CR-R-600 and CR-R-800 conditions. The

phase fraction of sigma phase decreases from 10% to 1 % for a change in annealing temperature from 600°C to 800°C HT condition. Based on the XRD measurements the L₂₁ phase was 6.4% in CR-R condition (no sigma phase, ductility is 60%), 13.2% in CR-R-600 condition (ductility is 25%) and 3.9% in CR-R-800 condition (ductility is 25%). Hence, it can be deduced that the effect of grain boundary sigma phase in CR-R-800 and CR-R-600 could be much severe compared to L₂₁. In CR-R-800 and CR-R-600, ductility can also be further affected by the size scale of L₁₂ particles due to change in deformation mechanism from cutting to bowing and dislocation interaction with the precipitates. The study also uses the thermodynamic modeling to rationalize the experimentally observed phase in this alloy, discussing the thermodynamical factors influencing the precipitation of equilibrium phases. Overall, the present study reveals the likelihood of developing novel precipitation strengthened HEAs with Cu clustering not only assisting in precipitation and stabilizing the second phase to higher temperature but also acting at a strengthening phase in the matrix.

5. Acknowledgements

The work was performed under a cooperative agreement between the Army Research Laboratory and the University of North Texas (W911NF-16-2-0189). The authors also acknowledge the DOE's Advanced Proton Source at the Argonne National Lab for providing access and user time on the beam line for x-ray diffraction experiments and would like to acknowledge Dr. Yang Ren for his support and guidance at the APS facility. The authors also acknowledge the Materials Research Facility (MRF) at the University of North Texas for use of microscopy and atom probe tomography facilities, and the Center for Electron Microscopy and Analysis (CEMAS) at the Ohio State University, for microscopy facilities.

Figure Captions

Figure 1. (a) Heat treatment routine and corresponding SEM images in $\text{Al}_{0.3}\text{Cu}_{0.3}\text{Ti}_{0.2}\text{CoCrFeNi}$. (b) BSED image from CR-R condition, (c) BSED image from CR-R-600, (d) BSED image from CR-R-800 condition. (b) Synchrotron XRD traces from the three HT condition of the $\text{Al}_{0.3}\text{Cu}_{0.3}\text{Ti}_{0.2}\text{CoCrFeNi}$ alloy.

Figure 2. TEM from CR-R: (a) BF image (b-d) SADPs from 112, 001, and 011 zone axes. (e-f) SADPs from 011 and 001 zone axes of the grain boundary precipitate respectively, (g) DF from the highlighted spots in (e) showing the L2_1 precipitate lighting up. (h) STEM image of the L2_1 precipitate (o-n) EDS maps showing the compositional partitioning across the precipitate and the matrix.

Figure 3. APT from CR-R: (a) reconstruction showing ion map of various elements as labeled - all ions, Al, Ni, Cu, Ti, Cr and Co. (b) One dimensional compositional profile across the arrow as marked in the Figure.

Figure 4. TEM from CR-R-600: (a-b) SADP from 100, 011 zone axis of fcc crystal structure respectively showing extra super-lattice spot. (d-g) STEM EDS maps of various elements as labeled.

Figure 5. TEM from CR-R-600: BF image showing the grain boundary region. (b-f) STEM EDS maps of various elements as labeled. (g) SADP from L21 (h) SADP from bcc and (i) SADP from B2 precipitate on the GB. (j) Overlayed elemental STEM maps for the different elements on one plot. (k) One dimensional compositional profile across the arrow as marked in the Figure.

Figure 6. APT from CR-R-600: (a) ion maps of various elements as labeled - all ions, Al, Ni, Cu, Ti, Cr and Co. (b) Left- the ion map with Cr ions in green color, Cu isosurface in orange color and Al isosurface in cyan color. (b)Right- proximity histogram across a 15% Al interface showing elemental partitioning between matrix and L1₂ phase and proximity histogram across a 25% Cu interface showing elemental partitioning between matrix and Cu rich phase.

Figure 7. TEM from CRS-A-800: (a) DFTEM image formed using the super-lattice spot highlighted in the SADP from [001]_{fcc} shown in the inset. (b) Another DFTEM image formed using the super-lattice spot highlighted in the SADP from [011]_{fcc} shown in the inset of this image.

Figure 8. Two-dimensional (2D) sections at (Al,Cu,Ti)0.8 for this septenary system corresponding to (a) 600°C and (b) 800°C, respectively.

Figure 9. (a)The phase fraction (mole fraction) of the different equilibrium phases as a function of temperature. For instance, at a temperature of 800°C, ThermoCalc predicts a $fcc\#2 + B2\#1 + \sigma$ (sigma) + $L1_2 + fcc\#1$ phase equilibria, $fcc\#2$ and $fcc\#1$ being (Fe,Co,Cr)-rich and Cu-rich (90at.%) according simulations, respectively. At 600 °C, ThermoCalc does not predict the presence of any equilibrium $L2_1$ phase at 600°C (as seen experimentally). Rather the thermodynamic modeling predicts two different B2 phases ($B2\#1$ and $B2\#2$), with phase fractions of 18% and 16% respectively. (b)The thermodynamic onset driving forces for the different phases at 600°C and 800°C.

Figure 10. Tensile testing of three different conditions, CR-R, CR-R-600 and CR-R-800: (a) Engineering stress-strain curves, (b) True stress-strain curves (inset shows the work-hardening rate versus true strain).

Supplementary Figure

Figure S1. Orientation image microscopy (OIM) showing the inverse pole figure and phase distribution in (a) CR-R-600 and (b) CR-R-800 conditions.

Table Captions

Table 1. Phase fraction and lattice parameters of different phases in three HT conditions in Al_{0.3}Cu_{0.3}Ti_{0.2}CoCrFeNi alloy measured using synchrotron XRD data.

Heat Treatment Condition	Phase			
	<i>fcc</i>	L2 ₁ /B2	L1 ₂	Sigma
CR-R	93.6	6.4	-	-
Phase Fraction (%)				
Lattice constant (Å)	3.61	5.83	-	-
CR-R-600/150h				
Phase Fraction (%)	42.7	13.2	34.2	10.1
Lattice constant (Å)	3.59	5.83	3.6	a=8.79, b=4.55
CR-R-800/0.5h				
Phase Fraction (%)	79.9	3.9	15.3	0.9
Lattice constant (Å)	3.6	5.84	3.6	a=8.79, b=4.55

Table 2 Compositions of various phases from STEM EDS results from in CR-R-600

Element	Cu rich (<i>fcc</i>)	Matrix (<i>fcc</i>)	σ	L2₁	L1₂	<i>bcc</i>
Al	2.12	4.06	1.72	12.71	12.16	3.74
Co	5.32	20.46	24.38	24.35	16.29	0.21
Cr	3.06	18.09	22.05	7.9	3.68	82.43
Ni	9.2	22.36	13.74	20.65	44.29	1.2
Fe	4.95	19.22	31.32	11.2	5.63	8.08
Ti	0.68	4.59	0.83	11.66	4.75	0.31
Cu	74.65	11.21	5.96	11.53	13.2	4.03

Table3. Compositions different phase from Atom probe results in CR-R-600 condition.

	Matrix	L1₂	Cu rich phase
Ion	Atomic Percent (%)		
Al	4.89	13.21	9.97
Ti	1.48	9.76	2.96
Fe	28.47	1.74	0.94
Ni	6.58	43.55	17.6
Co	24.52	15.35	4.19

Cu	0.68	15.93	64.23
Cr	33.38	0.46	0.12

References

- Yeh, J.W., S.K. Chen, S.J. Lin, J-Y. Gan, T.S. Chin, T.T. Shun, C.H. Tsau, and S.Y. Chang. "Nanostructured high-entropy alloys with multiple principal elements: novel alloy design concepts and outcomes." *Advanced Engineering Materials* 6, no. 5 (2004): 299-303.

2. Yeh, Jien Wei, Yu Liang Chen, Su Jien Lin, and Swe Kai Chen. "High-entropy alloys—a new era of exploitation." In Materials Science Forum, vol. 560, pp. 1-9. Trans Tech Publications, 2007.
3. B. Cantor, I.T.H. Chang, P. Knight, A.J.B. Vincent, Microstructural development in equiatomic multicomponent alloys, Mater. Sci. Eng. A 375e377 (2004) 213-218.
4. Jien-Wei, Y. "Recent progress in high entropy alloys." Ann. Chim. Sci. Mat 31, no. 6 (2006): 633-648.
5. Sheng, G. U. O., and Chain Tsuan LIU. "Phase stability in high entropy alloys: formation of solid-solution phase or amorphous phase." Progress in Natural Science: Materials International 21, no. 6 (2011): 433-446.
6. Miracle, Daniel B., Jonathan D. Miller, Oleg N. Senkov, Christopher Woodward, Michael D. Uchic, and Jaimie Tiley. "Exploration and development of high entropy alloys for structural applications." Entropy 16, no. 1 (2014): 494-525.
7. Zhang, Yong, Ting Ting Zuo, Zhi Tang, Michael C. Gao, Karin A. Dahmen, Peter K. Liaw, and Zhao Ping Lu. "Microstructures and properties of high-entropy alloys." Progress in Materials Science 61 (2014): 1-93.
8. Zhang, Y., Yang, X. & Liaw, P. K. Alloy Design and Properties Optimization of High-Entropy Alloys. JOM 64, 830–838 (2012).
9. Li, Dongyue, Chengxin Li, Tao Feng, Yidong Zhang, Gang Sha, John J. Lewandowski, Peter K. Liaw, and Yong Zhang. "High-entropy Al_{0.3}CoCrFeNi alloy fibers with high tensile strength and ductility at ambient and cryogenic temperatures." Acta Materialia 123 (2017): 285-294.

10. Shun, Tao-Tsung, and Yu-Chin Du. "Microstructure and tensile behaviors of FCC Al_{0.3}CoCrFeNi high entropy alloy." *Journal of Alloys and Compounds* 479, no. 1 (2009): 157-160.
11. Shun, Tao-Tsung, Cheng-Hsin Hung, and Che-Fu Lee. "Formation of ordered/disordered nanoparticles in FCC high entropy alloys." *Journal of Alloys and Compounds* 493, no. 1 (2010): 105-109.
12. Gwalani, B., V. Soni, D. Choudhuri, M. Lee, J. Y. Hwang, S. J. Nam, H. Ryu, S. H. Hong, and R. Banerjee. "Stability of ordered L1₂ and B₂ precipitates in face centered cubic based high entropy alloys-Al_{0.3}CoFeCrNi and Al_{0.3}CuFeCrNi₂." *Scripta Materialia* 123 (2016): 130-134.
13. Tang, Q. H., Y. Huang, Y. Y. Huang, X. Z. Liao, T. G. Langdon, and P. Q. Dai. "Hardening of an Al_{0.3}CoCrFeNi high entropy alloy via high-pressure torsion and thermal annealing." *Materials Letters* 151 (2015): 126-129.
14. Gwalani, B., Vishal Soni, Michael Lee, S. A. Mantri, Yang Ren, and R. Banerjee. "Optimizing the coupled effects of Hall-Petch and precipitation strengthening in a Al_{0.3}CoCrFeNi high entropy alloy." *Materials & Design* 121 (2017): 254-260.
15. Shun, Tao-Tsung, Cheng-Hsin Hung, and Che-Fu Lee. "The effects of secondary elemental Mo or Ti addition in Al 0.3 CoCrFeNi high-entropy alloy on age hardening at 700 C." *Journal of Alloys and Compounds* 495, no. 1 (2010): 55-58.
16. Jiang, Li, Yiping Lu, Yong Dong, Tongmin Wang, Zhiqiang Cao, and Tingju Li. "Annealing effects on the microstructure and properties of bulk high-entropy CoCrFeNiTi_{0.5} alloy casting ingot." *Intermetallics* 44 (2014): 37-43.

17. Gwalani, Bharat, Vishal Soni, Talukder Alam, and Raj Banerjee. "Designing and characterizing a complex concentrated gamma/gamma prime 'super-alloy'." *Microscopy and Microanalysis* 22, no. S3 (2016): 672-673.
18. Shun, T. T., Chang, L. Y. & Shiu, M. H. Microstructure and mechanical properties of multiprincipal component CoCrFeNiMox alloys. *Materials Characterization* 70, 63–67 (2012).
19. He, Feng, Zhijun Wang, Xuliang Shang, Chao Leng, Junjie Li, and Jincheng Wang. "Stability of lamellar structures in CoCrFeNiNb x eutectic high entropy alloys at elevated temperatures." *Materials & Design* 104 (2016): 259-264.
20. Wang, Z. G., W. Zhou, L. M. Fu, J. F. Wang, R. C. Luo, X. C. Han, B. Chen, and X. D. Wang. "Effect of coherent L12 nanoprecipitates on the tensile behavior of a fcc-based high-entropy alloy." *Materials Science and Engineering: A* 696 (2017): 503-510.
21. Liu, W. H., Z. P. Lu, J. Y. He, J. H. Luan, Z. J. Wang, B. Liu, Yong Liu, M. W. Chen, and C. T. Liu. "Ductile CoCrFeNiMo x high entropy alloys strengthened by hard intermetallic phases." *Acta Materialia* 116 (2016): 332-342.
22. He, Feng, Zhijun Wang, Sizhe Niu, Qingfeng Wu, Junjie Li, Jincheng Wang, C. T. Liu, and Yingying Dang. "Strengthening the CoCrFeNiNb 0.25 high entropy alloy by FCC precipitate." *Journal of Alloys and Compounds* 667 (2016): 53-57.
23. Liaw, Peter K. "Radiation Behavior of High-Entropy Alloys for Advanced Reactors." (2015).
24. Jiao, Zhi-Ming, Sheng-Guo Ma, Guo-Zheng Yuan, Zhi-Hua Wang, Hui-Jun Yang, and Jun-Wei Qiao. "Plastic Deformation of Al0. 3CoCrFeNi and AlCoCrFeNi High-Entropy

- Alloys Under Nanoindentation." *Journal of Materials Engineering and Performance* 24, no. 8 (2015): 3077-3083.
25. Li, Z., S. Zhao, H. Diao, P. K. Liaw, and M. A. Meyers. "High-velocity deformation of Al0. 3CoCrFeNi high-entropy alloy: Remarkable resistance to shear failure." *Scientific Reports* 7 (2017).
26. Shun, Tao-Tsung, and Yu-Chin Du. "Microstructure and tensile behaviors of FCC Al0.3CoCrFeNi high entropy alloy." *Journal of Alloys and Compounds* 479, no. 1 (2009): 157-160.
27. Ma, S. G., S. F. Zhang, M. C. Gao, P. K. Liaw, and Y. Zhang. "A successful synthesis of the CoCrFeNiAl0. 3 single-crystal, high-entropy alloy by Bridgman solidification." *Jom* 65, no. 12 (2013): 1751-1758.
28. Chen, Y. Y., T. Duval, U. D. Hung, J. W. Yeh, and H. C. Shih. "Microstructure and electrochemical properties of high entropy alloys—a comparison with type-304 stainless steel." *Corrosion science* 47, no. 9 (2005): 2257-2279.
29. Strutt, P. R., R. S. Polvani, and J. C. Ingram. "Creep behavior of the Heusler type structure alloy Ni 2 AlTi." *Metallurgical and Materials Transactions A* 7, no. 1 (1976): 23-31.
30. Gwalani, Bharat, Stephane Gorsse, Deep Choudhuri, Mark Styles, Yufeng Zheng, Rajiv S. Mishra, and Rajarshi Banerjee. "Modifying transformation pathways in High Entropy Alloys or Complex Concentrated Alloys via thermo-mechanical processing." *Acta Materialia* (2018).
31. Beltran, A. M., and D. A. Shores. "Super-alloys." *Wiley Interscience, New York* (1972): 317-339.

32. Pollock, Tresa M., and Sammy Tin. "Nickel-based super-alloys for advanced turbine engines: chemistry, microstructure and properties." *Journal of propulsion and power* 22, no. 2 (2006): 361-374.
33. Vanderwalker, D. M. "The precipitation sequence of Ni₃Ti in Co-free maraging steel." *Metallurgical Transactions A* 18, no. 7 (1987): 1191-1194.
34. Jiao, Zengbao, and Chain-Tsuan Liu. "Ultrahigh-strength steels strengthened by nanoparticles." *Science Bulletin* 62, no. 15 (2017): 1043-1044.
35. Chuang, Ming-Hao, Ming-Hung Tsai, Woei-Ren Wang, Su-Jien Lin, and Jien-Wei Yeh. "Microstructure and wear behavior of Al_xCo_{1.5}Cr_{Fe}Ni_{1.5}Tiy high-entropy alloys." *Acta Materialia* 59, no. 16 (2011): 6308-6317.
36. Shun, Tao-Tsung, Cheng-Hsin Hung, and Che-Fu Lee. "The effects of secondary elemental Mo or Ti addition in Al_{0.3}CoCrFeNi high-entropy alloy on age hardening at 700 C." *Journal of Alloys and Compounds* 495, no. 1 (2010): 55-58.
37. He, J. Y., H. Wang, H. L. Huang, X. D. Xu, M. W. Chen, Y. Wu, X. J. Liu, T. G. Nieh, K. An, and Z. P. Lu. "A precipitation hardened high-entropy alloy with outstanding tensile properties." *Acta Materialia* 102 (2016): 187-196.
38. Guo, Sheng, Chun Ng, and Chain Tsuan Liu. "Anomalous solidification microstructures in Co-free Al_xCrCuFeNi₂ high-entropy alloys." *Journal of Alloys and Compounds* 557 (2013): 77-81.
39. Gwalani, B., D. Choudhuri, V. Soni, Y. Ren, M. Styles, J. Y. Hwang, S. J. Nam, H. Ryu, S. H. Hong, and R. Banerjee. "Cu assisted stabilization and nucleation of L1₂ precipitates in Al_{0.3}CuFeCrNi₂ fcc-based high entropy alloy." *Acta Materialia* 129 (2017): 170-182.

40. JY, Yoo, and Choo WY. "Microstructures and age hardening characteristics of direct quenched Cu bearing HSLA steel." *ISIJ international* 35, no. 8 (1995): 1034-1040.
41. Vaynman, Semyon, Dieter Isheim, R. Prakash Kolli, Shrikant P. Bhat, David N. Seidman, and Morris E. Fine. "High-strength low-carbon ferritic steel containing Cu-Fe-Ni-Al-Mn precipitates." *Metallurgical and Materials Transactions A* 39, no. 2 (2008): 363-373.
42. Hammersley, A. P. "FIT2D: an introduction and overview." *European Synchrotron Radiation Facility Internal Report ESRF97HA02T* 68 (1997): 58.
43. Young, M. L., J. D. Almer, M. R. Daymond, D. R. Haeffner, and D. C. Dunand. "Load partitioning between ferrite and cementite during elasto-plastic deformation of an ultrahigh-carbon steel." *Acta materialia* 55, no. 6 (2007): 1999-2011.
44. Lutterotti, Luca, S. Matthies, and H. Wenk. "MAUD: a friendly Java program for material analysis using diffraction." *CPD NEWSLETTER* 21 (1999): 14-15.
45. Gražulis, Saulius, Daniel Chateigner, Robert T. Downs, A. F. T. Yokochi, Miguel Quirós, Luca Lutterotti, Elena Manakova, Justas Butkus, Peter Moeck, and Armel Le Bail. "Crystallography Open Database—an open-access collection of crystal structures." *Journal of Applied Crystallography* 42, no. 4 (2009): 726-729.
46. Wyckoff, Ralph WG. "Cubic closest packed, ccp." *Structure, Cryst. Struct* 1 (1963): 7-83.
47. Wyckoff, Ralph WG. *The structure of crystals*. The Chemical Catalog Co, Inc.; New York, 1931.
48. Wyckoff, Ralph WG. *The structure of crystals*. The Chemical Catalog Co, Inc.; New York, 1931.

49. Yakel, H. L. "Atom distributions in sigma phases. I. Fe and Cr atom distributions in a binary sigma phase equilibrated at 1063, 1013 and 923 K." *Acta Crystallographica Section B: Structural Science* 39, no. 1 (1983): 20-28.
50. Kurt, H., and J. M. D. Coey. "Heusler Alloys: Properties, Growth, Applications." (2016): 157-192.
51. Choudhuri, D., T. Alam, T. Borkar, B. Gwalani, A. S. Mantri, S.G. Srinivasan, M. A. Gibson, and R. Banerjee. "Formation of a Huesler-like L21 phase in a CoCrCuFeNiAlTi high-entropy alloy." *Scripta Materialia* 100 (2015): 36-39.
52. Hsieh, Chih-Chun, and Weite Wu. "Overview of Intermetallic Sigma (σ) Phase Precipitation in Stainless Steels." *ISRN Metallurgy* 2012 (2012).
53. Rao, J. C., H. Y. Diao, V. Ocelík, D. Vainchtein, C. Zhang, C. Kuo, Z. Tang et al. "Secondary phases in Al x CoCrFeNi high-entropy alloys: An in-situ TEM heating study and thermodynamic appraisal." *Acta Materialia* 131 (2017): 206-220.
54. Tsai, Ming-Hung, Hao Yuan, Guangming Cheng, Weizong Xu, Weiwei W. Jian, Ming-Hao Chuang, Chien-Chang Juan, An-Chou Yeh, Su-Jien Lin, and Yuntian Zhu. "Significant hardening due to the formation of a sigma phase matrix in a high entropy alloy." *Intermetallics* 33 (2013): 81-86.
55. Soffa, W. A., and D. E. Laughlin. "Decomposition and ordering processes involving thermodynamically first-order order→ disorder transformations." *Acta Metallurgica* 37, no. 11 (1989): 3019-3028.
56. Rojhirunsakool, Tanaporn, Soumya Nag, and Rajarshi Banerjee. "Discontinuous precipitation of γ' phase in Ni-Co-Al Alloys." *JOM* 66, no. 8 (2014): 1465-1470.

57. Williams, D. B., and E. P. Butler. "Grain boundary discontinuous precipitation reactions." International Metals Reviews 26, no. 1 (1981): 153-183.
58. O. Senkov, J. Miller, D. Miracle and C. Woodward: Accelerated exploration of multiprincipal element alloys with solid solution phases. Nature Communications 6:6529 (2015)
59. Asgari, Sorous, Ehab El-Danaf, Surya R. Kalidindi, and Roger D. Doherty. "Strain hardening regimes and microstructural evolution during large strain compression of low stacking fault energy fcc alloys that form deformation twins." Metallurgical and Materials Transactions A 28, no. 9 (1997): 1781-1795.
60. El-Danaf, Ehab, Surya R. Kalidindi, and Roger D. Doherty. "Influence of grain size and stacking-fault energy on deformation twinning in fcc metals." Metallurgical and Materials Transactions A 30, no. 5 (1999): 1223-1233.
61. Jin, Jae-Eun, and Young-Kook Lee. "Strain hardening behavior of a Fe–18Mn–0.6 C–1.5 Al TWIP steel." Materials Science and Engineering: A 527, no. 1-2 (2009): 157-161.
62. Ding, Hao, Hua Ding, Dan Song, Zhengyou Tang, and Ping Yang. "Strain hardening behavior of a TRIP/TWIP steel with 18.8% Mn." Materials Science and Engineering: A 528, no. 3 (2011): 868-873

Authors Contributions

BG designed the research and conducted the SEM, TEM and APT examination. SG conducted the thermodynamic assessment using Calphad. YZ conducted CHEMI-STEM imaging. VS, AV helped in sample preparation. MC, NL, MY did the XRD experiments and analysis. MY, RM and

RB supervised and guided the research. All authors discussed and helped in framing the manuscript. BG, SG and RB wrote the manuscript.

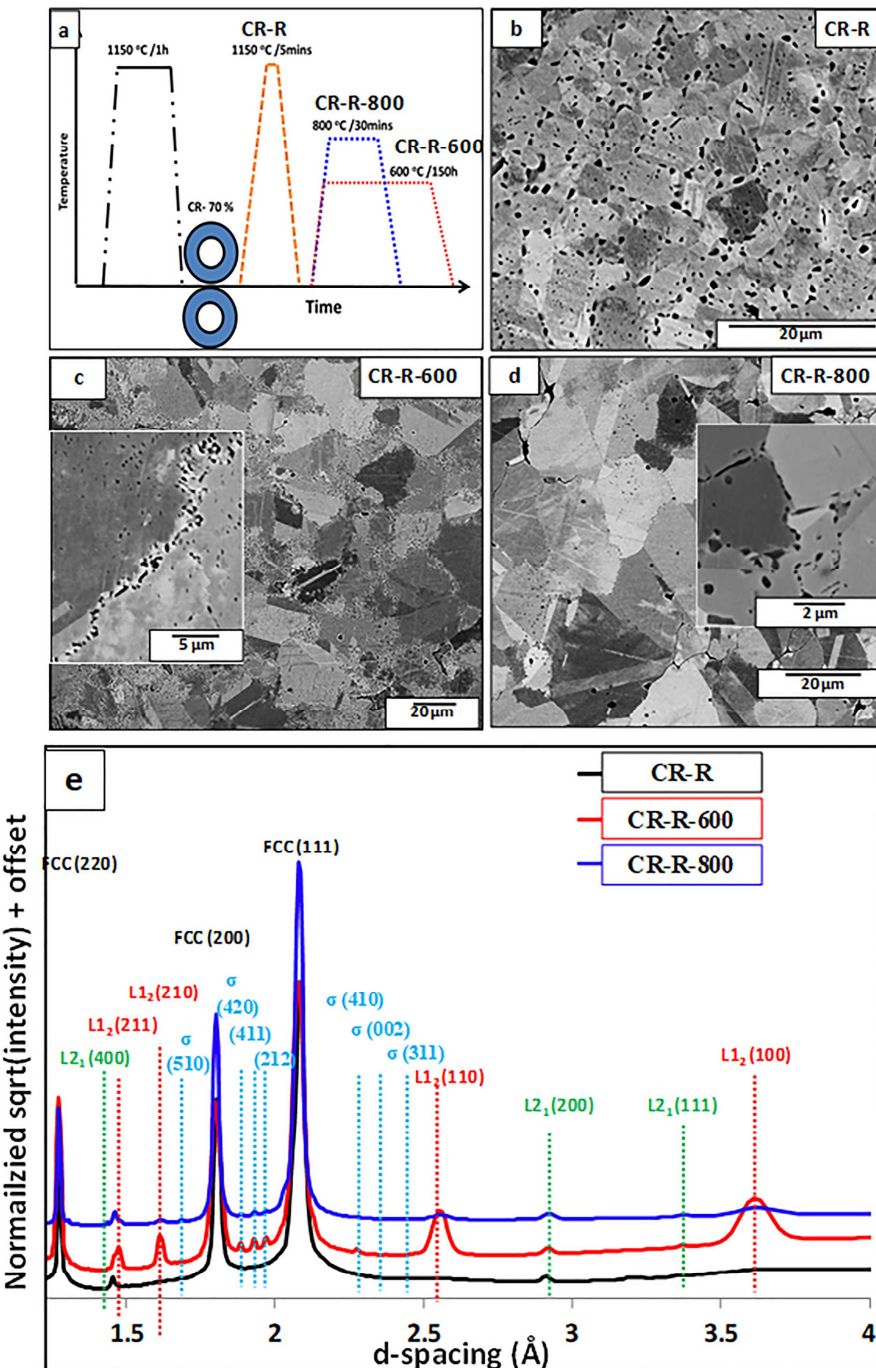


Figure 1. (a) Heat treatment routine and corresponding SEM images in $\text{Al}_{0.3}\text{Cu}_{0.3}\text{Ti}_{0.2}\text{CoCrFeNi}$. (b) BSED image from CR-R condition, (c) BSED image from CR-R-600, (d) BSED image from CR-R-800 condition. (e) Synchrotron XRD traces from the three HT condition of the $\text{Al}_{0.3}\text{Cu}_{0.3}\text{Ti}_{0.2}\text{CoCrFeNi}$ alloy.

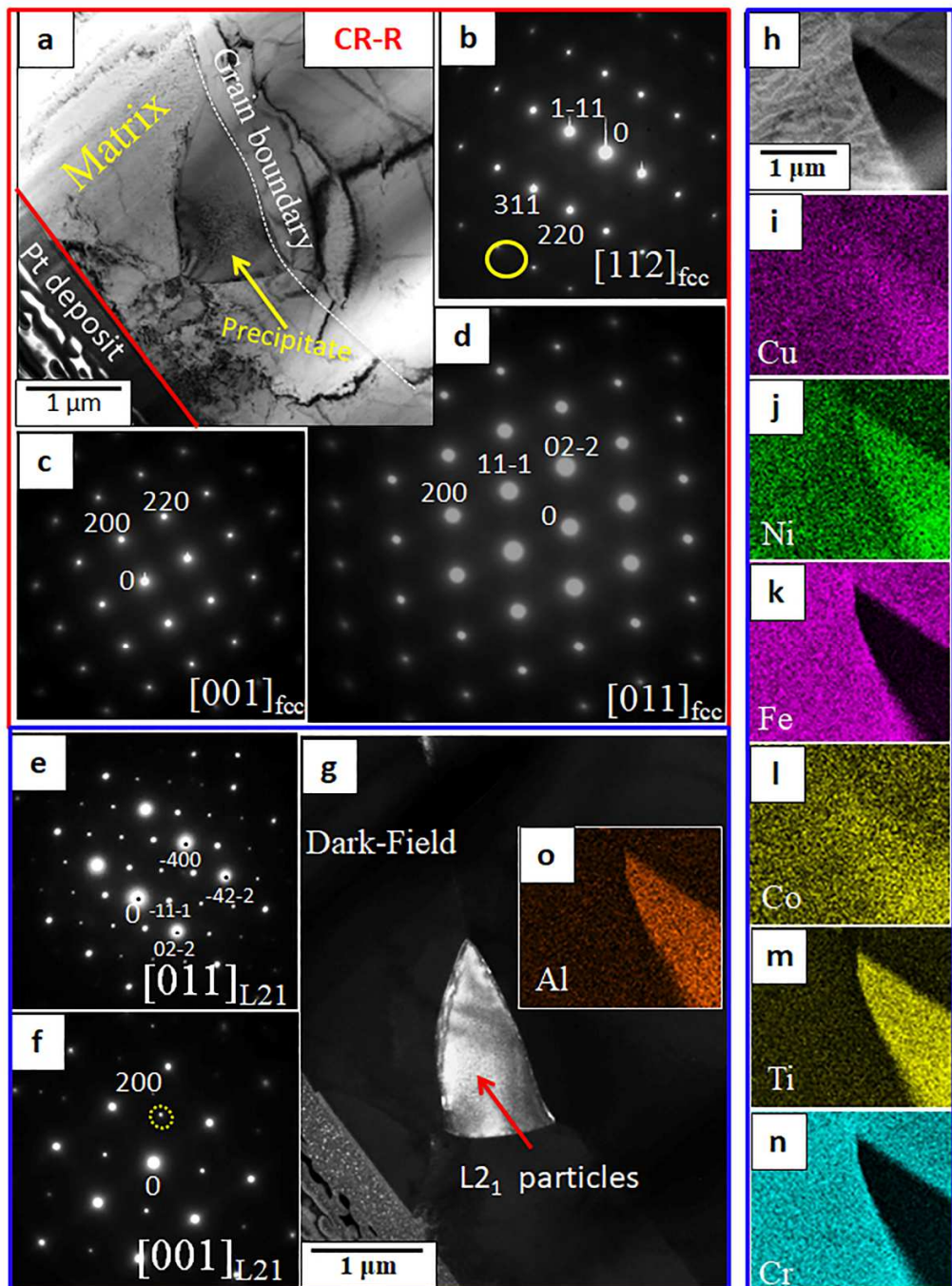


Figure 2. TEM from CR-R: (a) BF image (b-d) SADPs from 112, 001, and 011 zone axes. (e-f) SADPs from 011 and 001 zone axes of the grain boundary precipitate respectively, (g) DF from the highlighted spots in (e) showing the L₂₁ precipitate lighting up. (h) STEM image of the L₂₁ precipitate (o-n) EDS maps showing the compositional partitioning across the precipitate and the matrix.

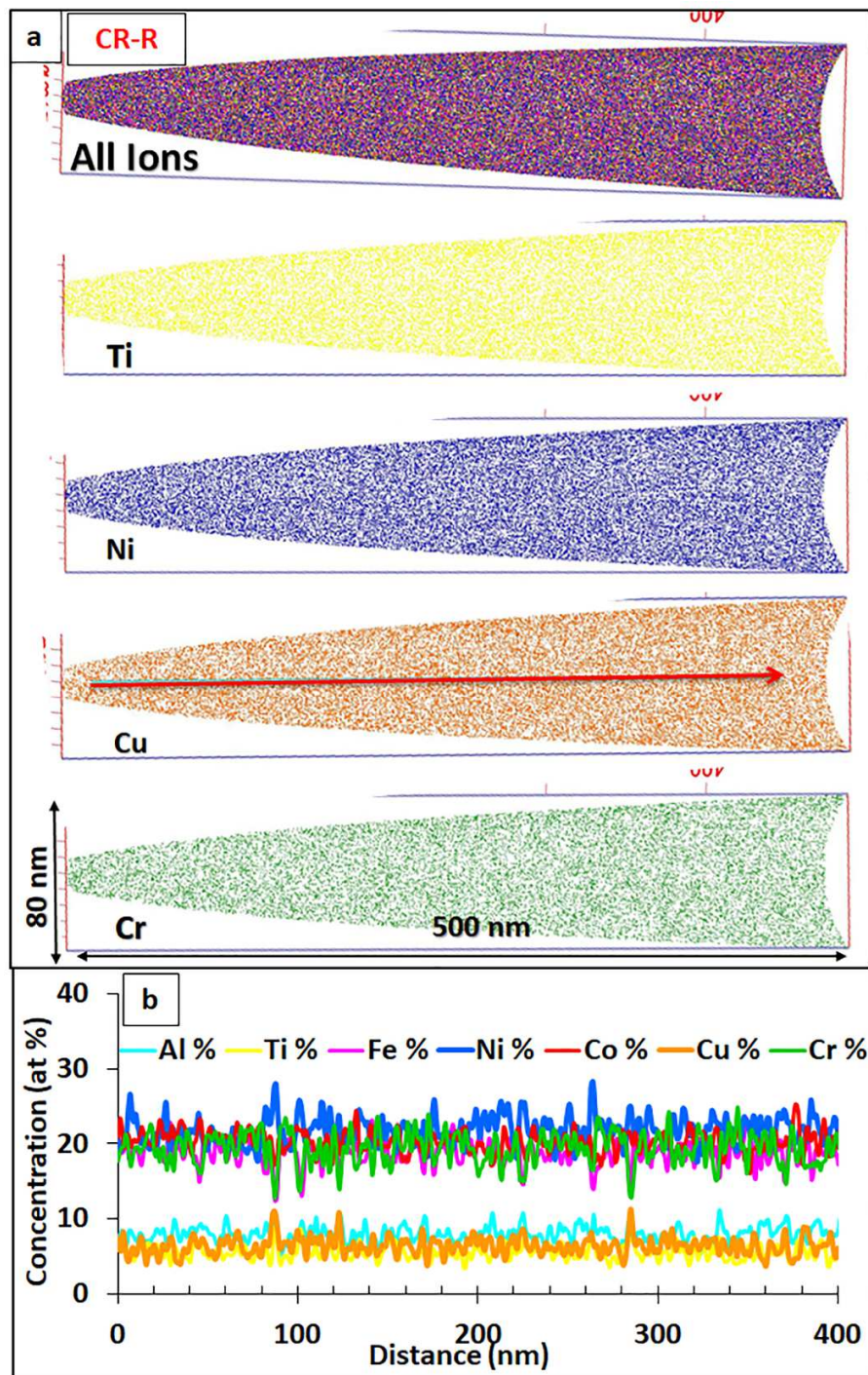
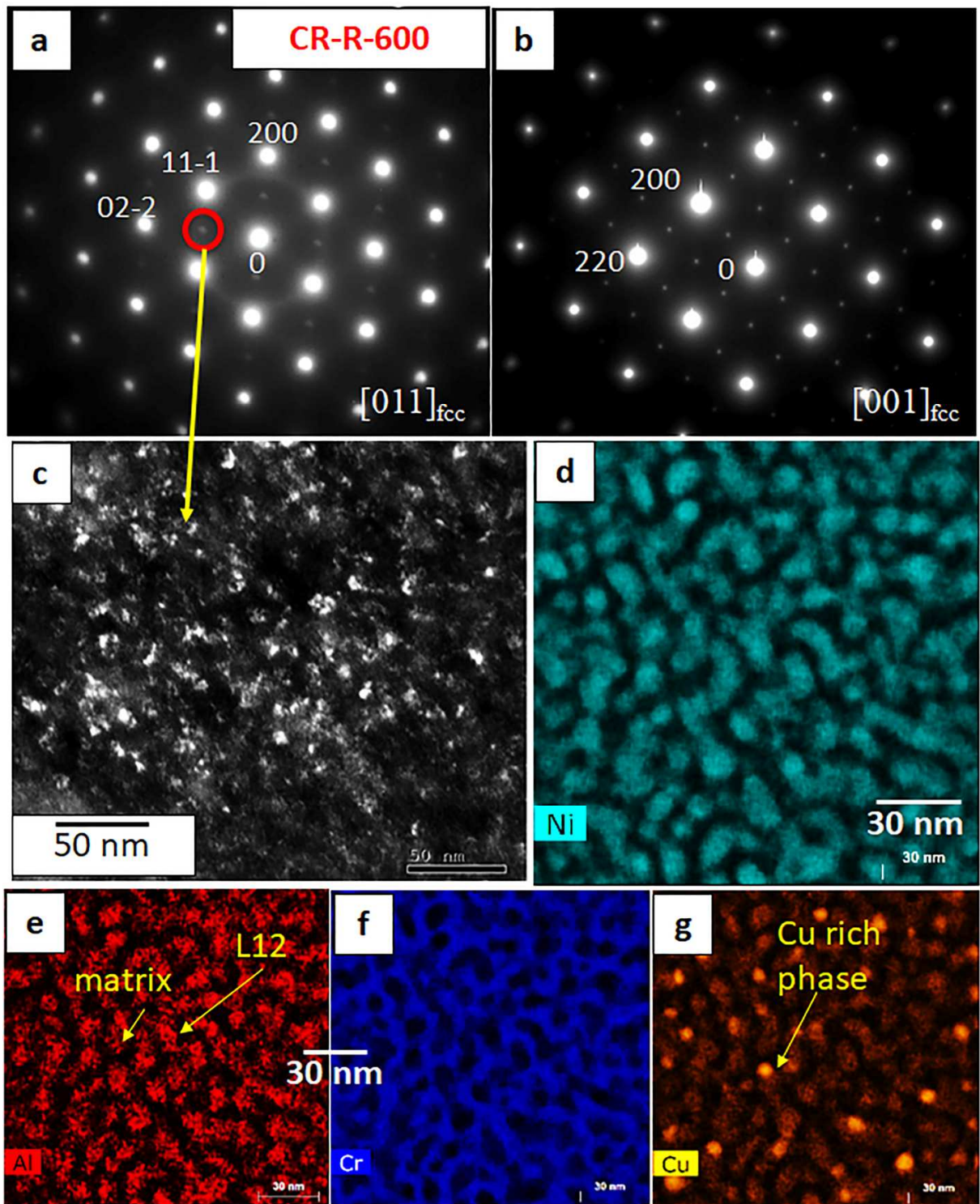


Figure 3. APT from CR-R: (a) reconstruction showing ion map of various elements as labeled - all ions, Al, Ni, Cu, Ti, Cr and Co. (b) One dimensional compositional profile across the arrow as marked in the Figure.



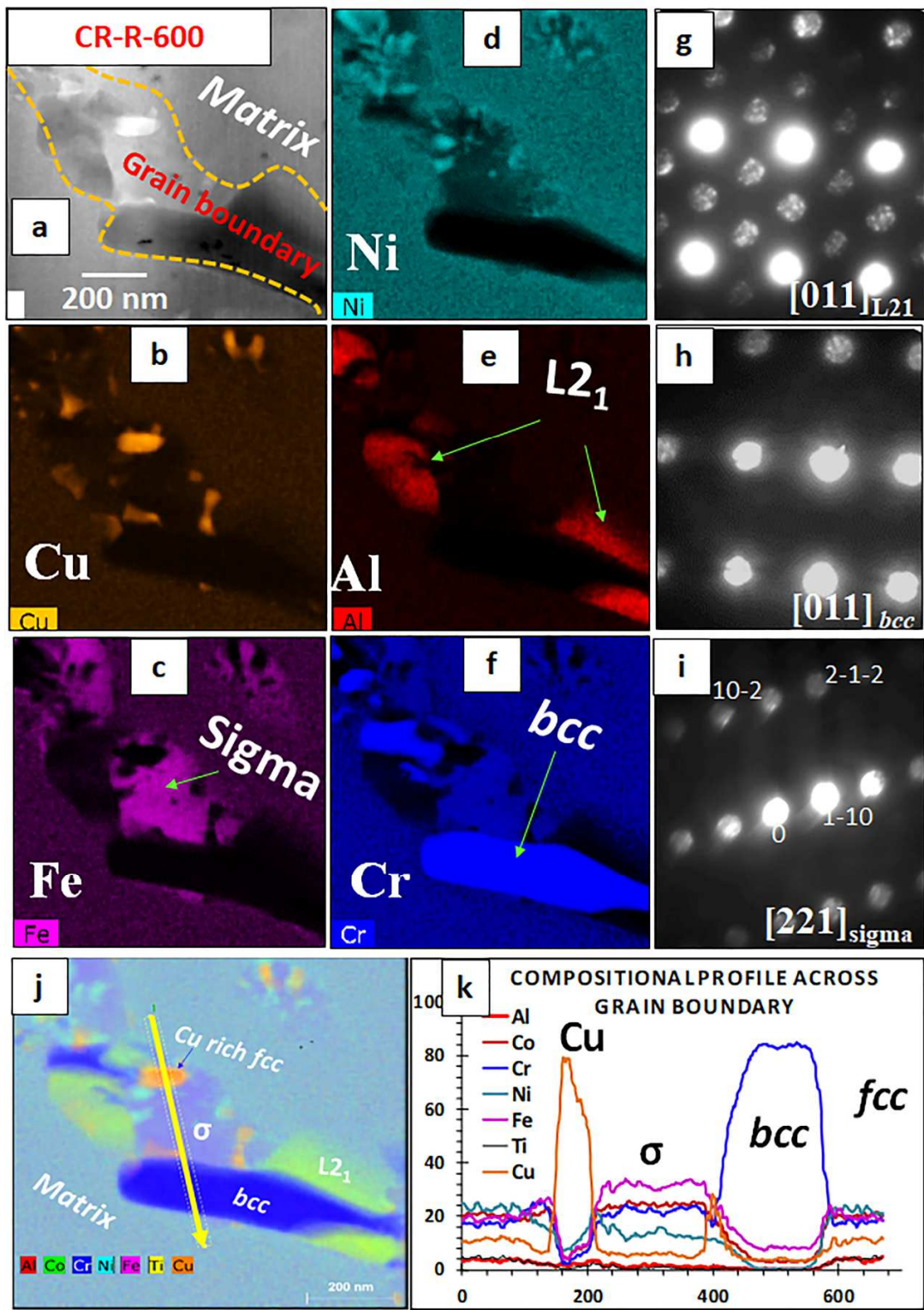


Figure 5. TEM from CR-R-600: BF image showing the grain boundary region. (b-f) STEM EDS maps of various elements as labeled. (g) SADP from L21 (h) SADP from bcc and (i) SADP from B2 precipitate on the GB. (j) Overlaid elemental STEM maps for the different elements on one plot. (k) One dimensional compositional profile across the arrow as marked in the Figure.

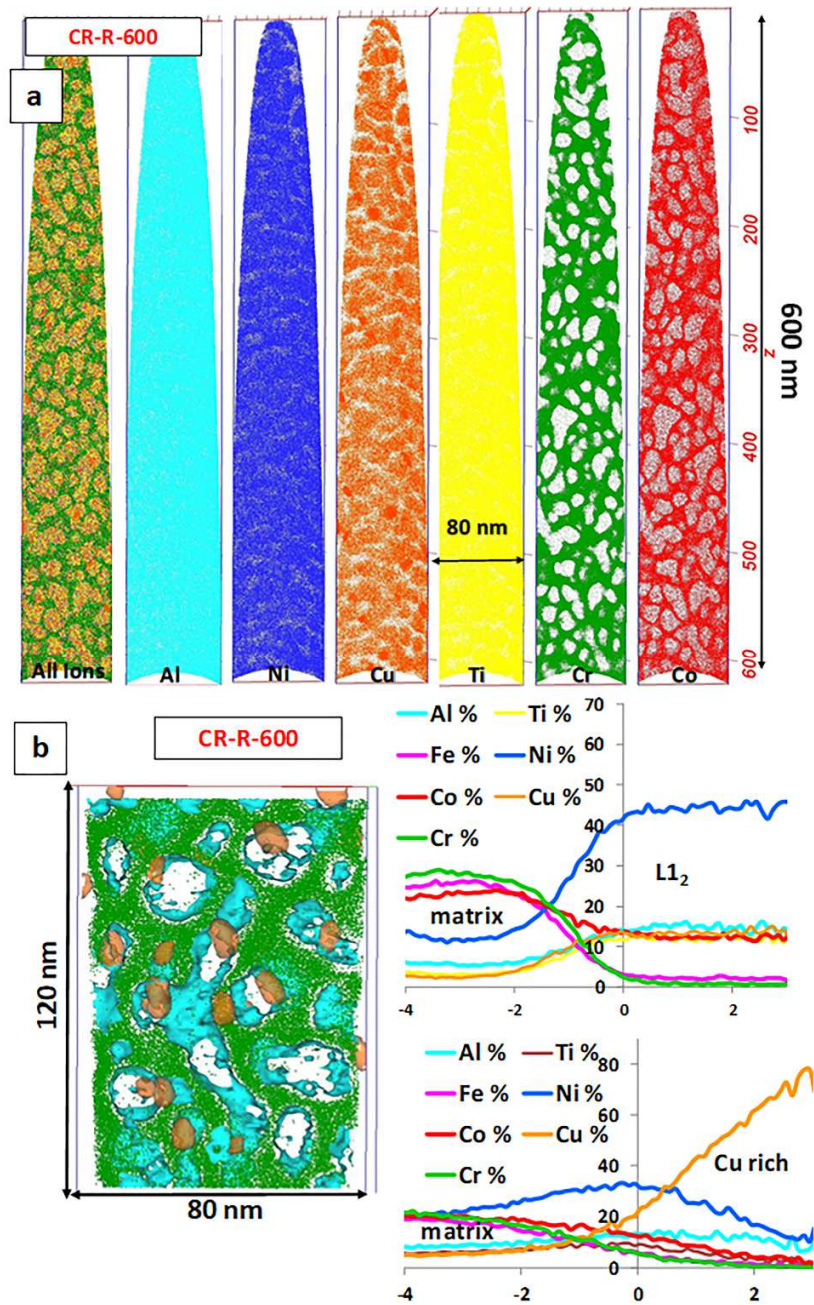


Figure 6. APT from CR-R-600: (a) ion maps of various elements as labeled - all ions, Al, Ni, Cu, Ti, Cr and Co. (b) Left- the ion map with Cr ions in green color, Cu isosurface in orange color and Al isosurface in cyan color. (b)Right- proximity histogram across a 15% Al interface showing elemental partitioning between matrix and $L1_2$ phase and proximity histogram across a 25% Cu interface showing elemental partitioning between matrix and Cu rich phase.

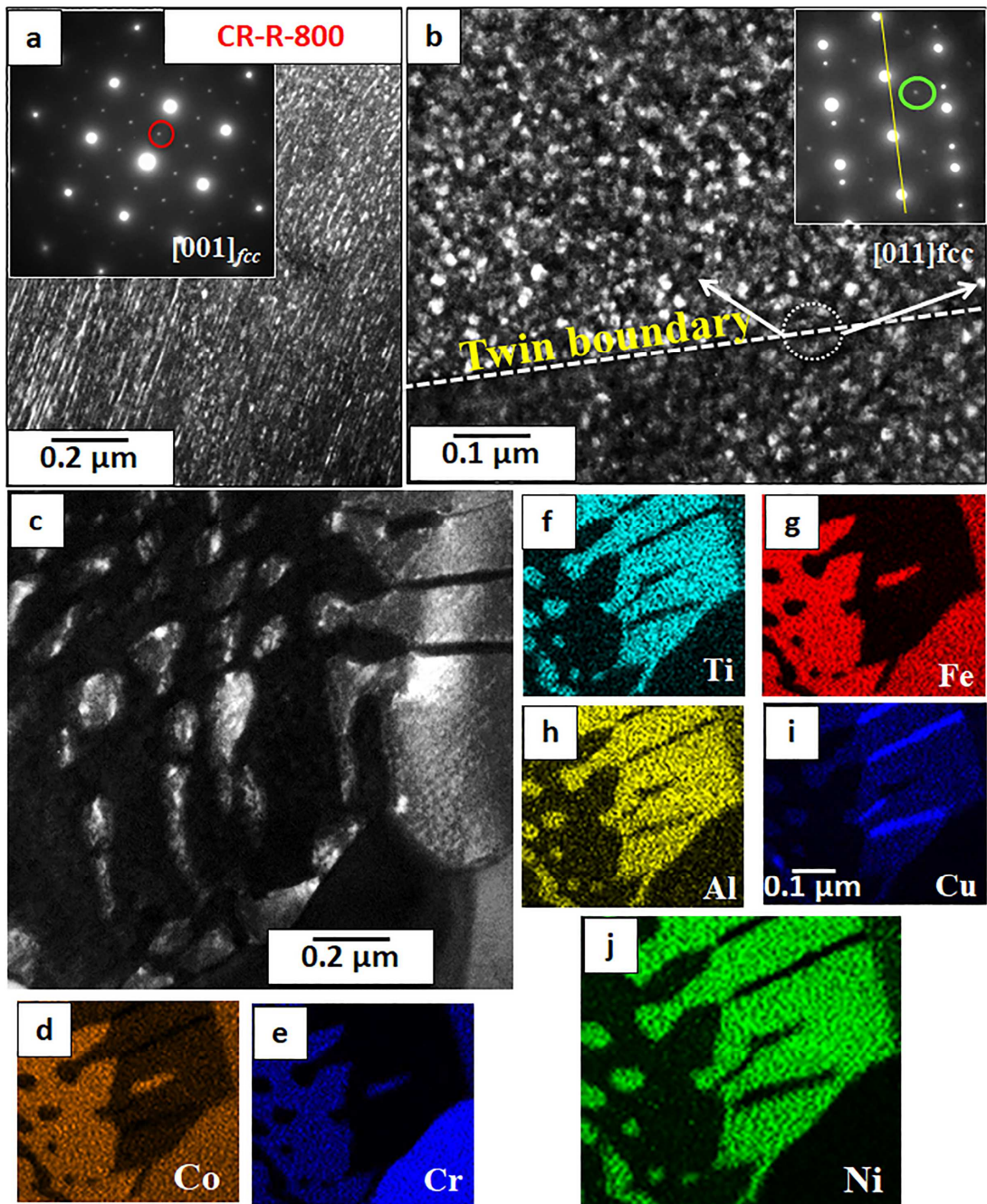


Figure 7. TEM from CRSA-800: (a) DFTEM image formed using the super lattice spot highlighted in the SADP from $[001]_{fcc}$ shown in the inset. (b) Another DFTEM image formed using the super lattice spot highlighted in the SADP from $[011]_{fcc}$ shown in the inset of this image.

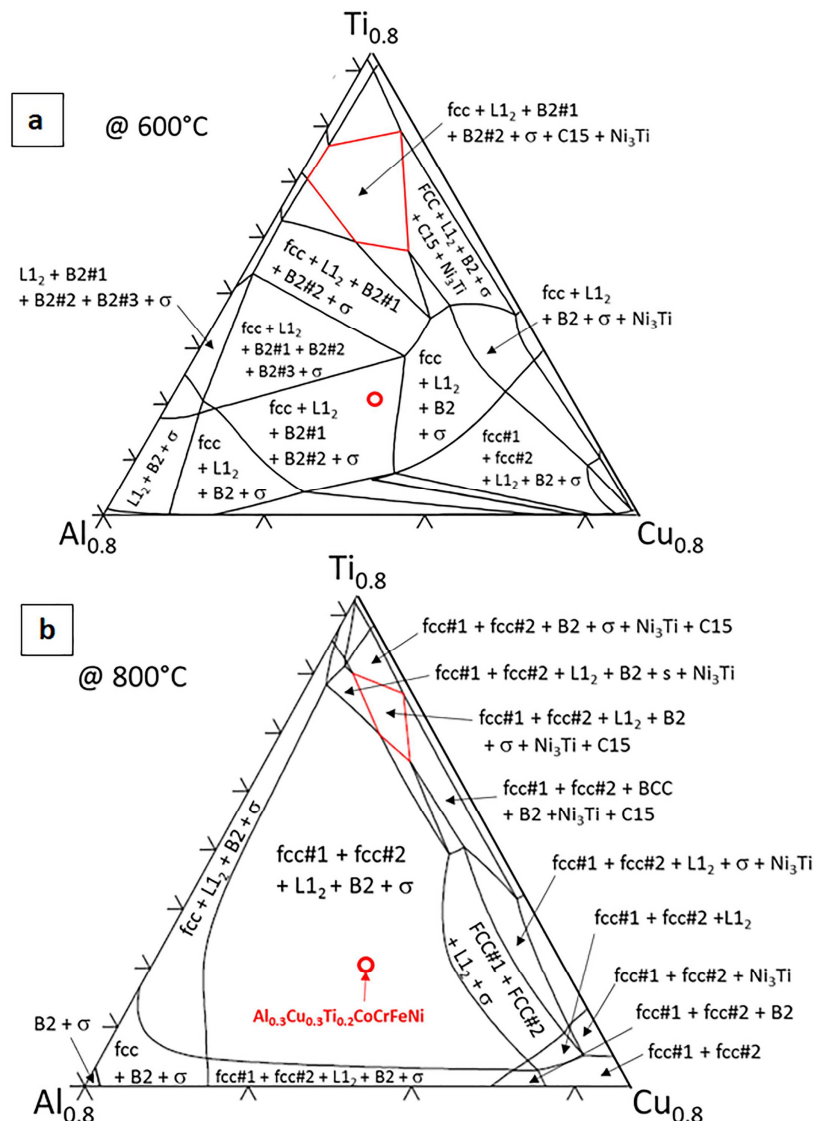


Figure 8. Two-dimensional (2D) sections at $(\text{Al}, \text{Cu}, \text{Ti})0.8$ for this septenary system corresponding to (a) 600°C and (b) 800°C, respectively.

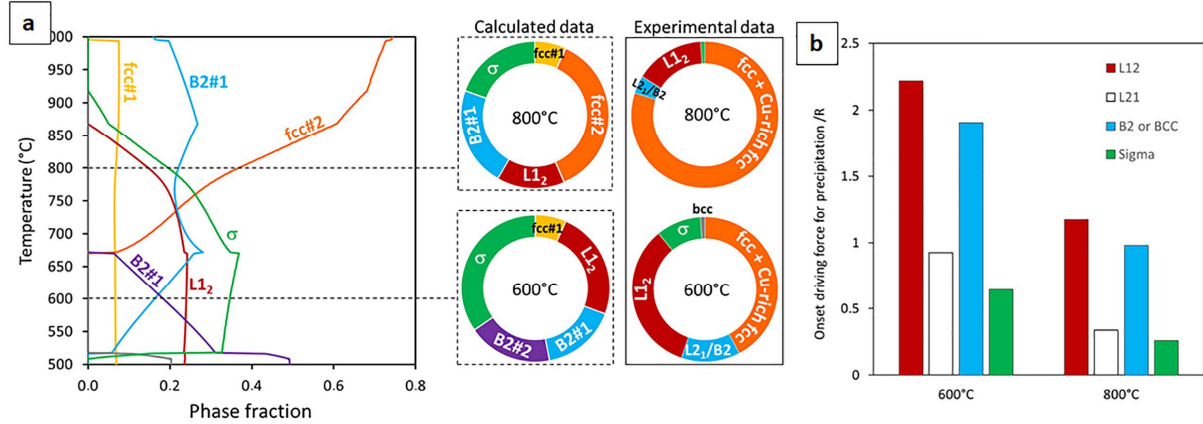


Figure 9. (a) The phase fraction (mole fraction) of the different equilibrium phases as a function of temperature. For instance, at a temperature of 800°C, ThermoCalc predicts a $fcc\#2 + B2\#1 + \sigma(\sigma)$ + $L1_2 + fcc\#1$ phase equilibria, $fcc\#2$ and $fcc\#1$ being (Fe,Cu,Cr)-rich and Cu-rich (90at.%) according simulations, respectively. At 600 °C, ThermoCalc does not predict the presence of any equilibrium $L2_1$ phase at 600°C (as seen experimentally). Rather the thermodynamic modeling predicts two different B2 phases ($B2\#1$ and $B2\#2$), with phase fractions of 18% and 16% respectively. (b) The thermodynamic onset driving forces for the different phases at 600°C and 800°C.

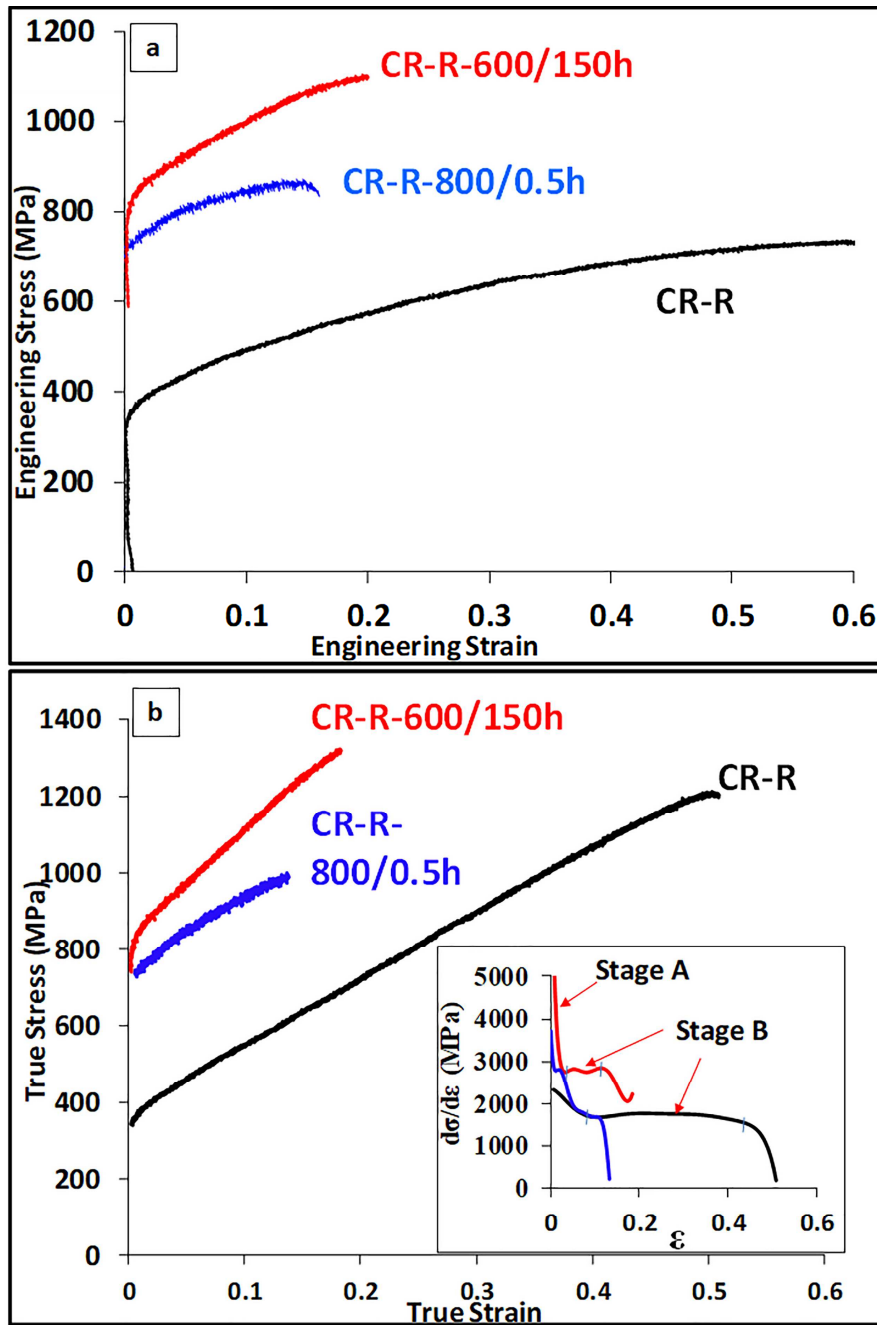


Figure 10. Tensile testing of three different conditions, CR-R, CR-R-600 and CR-R-800: (a) Engineering stress-strain curves, (b) True stress-strain curves (inset shows the work-hardening rate versus true strain).

CR-R-600/150h

